Contents lists available at ScienceDirect

Materials Today Nano

Angstrom-scale replication of surfaces with crystallized bulk metallic glasses

Z. Chen [a], Y. Xie [a], A. Datye [a, *], J. Thornton [b], J. Schroers [a], J.J. Cha [a], U.D. Schwarz [a, c, **]

[a] Department of Mechanical Engineering and Materials Science, Yale University, New Haven, CT, 06511, USA
[b] Bruker Nano Surfaces, Billerica, MA, 01821, USA
[c] Department of Chemical and Environmental Engineering, Yale University, New Haven, CT, 06511, USA

ARTICLE INFO

ABSTRACT

The replication of single-crystalline strontium titanate (STO) surfaces through thermoplastic forming with a $Pt_{57.5}Cu_{14.7}Ni_{5.3}P_{22.5}$ alloy that is in a glassy state during forming but subsequently heated *in situ* until crystallized is investigated. In contrast to postforming *ex situ* heating to crystallization, which roughens the surface, atomic force microscopy measurement of replicas that crystallize while still being in contact with the mold reveals an exact angstrom-scale replication of the terraced surface features found on the STO molds. The structure and degree of crystallinity of the metallic replicas is characterized by x-ray diffraction, differential scanning calorimetry, and high-resolution transmission electron microscopy. Thereby, it is found that even though the bulk of the sample fully crystallizes, a thin surface layer remains partly amorphous despite extended heating above typical bulk crystallization temperatures and times. The existence of this layer is not only key to overcome the intrinsic limits of replication accuracy that would be imposed by the lattice parameters if the alloy were to fully crystallize but also expected to improve many of the part's mechanical and chemical properties while the crystalline bulk provides stability at elevated temperatures.

1. Introduction

Nanoimprinting is exploited as an economical alternative to − or in combination with − optical and electron-beam lithography to create nanoscale features on materials for optical, electronic, chemical, and biological applications [1−8]. It is particularly suitable for materials that feature a glass transition such as polymers and metallic glasses, which enables high-accuracy imprinting via thermoplastic forming or hot embossing when the material is heated above its glass transition temperature [9−11]. This technique could also be applied to generate nanopatterns on other materials when applying novel shaping mechanisms such as laser shock or direct superplastic and electrochemical imprinting to adapt metals or semiconductors to molds [12−14]. The limitation of imprinting accuracy is usually caused by the forming material's plastic forming capabilities such as its viscosity at imprinting

temperature and any intrinsic size scale imposed by the material's individual flow units (e.g., size of molecules in polymers or grain sizes in crystalline metals) [12]. As a consequence, the imprinting accuracy of polymers has reached the nanometer scale while the one for crystalline metals is at around ten nanometers [10,12,13,15−18].

Bulk metallic glasses (BMGs), however, have no intrinsic size limit larger than the atoms they consist of and were shown to be able to accurately replicate surface features of suitable molds at the atomic scale [19,20]. More specifically, the height of surface steps separating individual atomic terraces of single-crystal ceramic molds could be reproduced with subangstrom precision irrespective of the exact height of the steps, a quality that is assigned to the fact that features on surfaces of amorphous metals do not need to conform with specific dimensions imposed by nearest-neighbor distances or unit cell sizes that govern topographies exposed by crystalline materials. Thus, it can be regarded as a unique property of fully amorphous metallic glasses to replicate a crystalline mold's well-defined atomic step structure with subangstrom precision (note that while silica glasses have successfully been used to emboss step structures, they so far lack the impressive accuracy

* Corresponding author.
** Corresponding author.
E-mail addresses: amit.datye@yale.edu (A. Datye), udo.schwarz@yale.edu (U.D. Schwarz).

displayed by metallic glasses [21–23]). Here, we demonstrate a novel way of generating imprints of the terraced atomic surface structure of a ceramic substrate where a fully crystalline bulk is covered by a thin, largely disordered surface layer that provides the same outstanding accuracy of surface replication as samples that are entirely glassy do. Because amorphous alloys have better tensile strength, fatigue strength, and wear and corrosion resistance compared to their crystalline counterparts [24,25], the sample's mechanical and chemical performance is expected to be superior to a part that would be fully crystalline while the crystalline bulk provides the sample with better structural stability at elevated temperatures compared to a fully amorphous workpiece. Combined, these characteristics make the method attractive for applications such as fuel cells, devices that feature moving parts at the nanoscale, hierarchical nanopatterning for adhesion or wear control, surface templating for material growth, and so on.

2. Experimental method

2.1. Mold preparation

One side polished strontium titanate (STO) (100) single crystals were purchased from MTI Corporation (Richmond, CA, USA). As we have shown in pervious publications [7,19,26–28], surface morphology featuring atomically flat TiO_2-terminated terraces separated by steps of one unit cell height (i.e., 0.3905 nm) was achieved from these crystals through ultrasonic agitation in distilled water for 10 min followed by annealing in a Carbolite tube furnace with airflow at 1000 °C for two hours [26,29].

2.2. Imprinting and crystallization

A cylindrical ingot of $Pt_{57.5}Cu_{14.7}Ni_{5.3}P_{22.5}$ bulk metallic glass (Pt-BMG) was used as the precursor material for the ultimately crystalline replica using settings similar to ones we have reported earlier for the atomic-scale imprinting of the same material yielding amorphous duplication [19]. In short, an Instron 5569 mechanical testing machine with customized heating plates controlling a precise temperature environment at 270 °C ± 0.5 °C was used to apply the imprinting pressure. To carry out the forming, an STO mold prepared as described earlier was positioned on the Instron's lower heating plate. Once the heating plates and STO mold all had reached a steady-state temperature, a Pt-BMG ingot was placed on the STO mold. Following a waiting period of ≈30 s to allow the Pt-BMG ingot to equilibrate at 270 °C, the load was gradually increased to 1000 N ± 1 N at a loading rate of 6 N/s. This maximum load was then kept for 3 min if amorphous replicas were desired, but for samples to crystallize, the holding time was extended to 20 min, 30 min, and 40 min, respectively, for three different batches of samples. For further insight, a fourth batch of samples was prepared where after 3 min hold time at 270 °C and maximum load, the temperature of the plates was increased to 450 °C ± 0.5 °C within about 2 min and subsequently kept at that temperature for 5 min. After the sample-specific heating and hold procedure was completed and load had been released, samples were quickly cooled down by placing them on a large room temperature bronze plate. Replicas could then easily be separated from their respective molds.

2.3. Sample characterization

Topographical atomic force microscopy (AFM) characterization of the imprinted surface was conducted in ambient condition using Bruker Multimode AFM operated in tapping mode with Nanoscope III electronics. Thereby, Bruker RTESPAW-300 silicon cantilevers were used at driving frequencies ranging from 290 kHz to 300 kHz, and Root Mean Square (RMS) surface roughness values were determined by averaging the results obtained from three squared on-terrace areas of 50 nm × 50 nm each taken at different locations on the sample.

Viscoelastic mapping of the samples was performed using the FASTForce Volume CR (contact resonance) technique on Bruker Dimension ICON AFM. In this method, the cantilever vibrates in dynamic contact while monitoring the contact resonance frequency to measure the storage modulus E', the loss modulus E'', and the loss tangent. Toward this end, the sample is mounted on an actuator to provide mechanical vibration as in atomic force acoustic microscopy [30]. By monitoring the frequency and quality factor of the contact resonance peak, both the stiffness and energy dissipation can be determined and used in the storage and loss modulus calculations, respectively. The implementation used in this study uses the force volume to position the probe during a force curve at each pixel in the image, sweep the frequency to visualize the entire contact resonance peak at the primary contact resonance or a higher eigenmode, and then make measurements from each spectrum acquired [31]. The measurements were performed with a diamond-coated silicon single-beam cantilever from Bruker, Model DDLTESP-V2, with a natural resonance frequency of 225 kHz and a nominal spring constant of 65 N/m.

Differential scanning calorimeter (DSC) measurements of the samples in the main text were conducted with a Perkin Elmer Precisely Diamond DSC, while the DSC measurements shown in Fig. S2 in the supplementary are carried out on a TA Instruments DSC Q200. X-ray diffraction (XRD) measurements were carried out using a Rigaku SmartLab X-ray diffractometer. For the cross-sectional transmission electron microscopy (TEM) analysis, thin lamella samples were cut from the replica using a focused ion beam scanning electron microscope (FIB-SEM, FEI Helios G4 UX Dual-Beam). To preserve the surface of the replica, a 2-μm-thick carbon layer was first deposited on the surface of the replica inside the FIB-SEM but before the ion milling started. The sample was subsequently thinned down to form a lamella of around 80 nm thickness using an acceleration voltage of 5 kV and a current of 64 pA. The cross-sectional TEM images and nanobeam diffraction patterns were then acquired at the Advanced Science Research Center of the City University of New York using a FEI Titan Themis TEM operated with an acceleration voltage of 200 kV.

3. Results and discussion

Fig. 1 presents an analysis of four replica made from $Pt_{57.5}Cu_{14.7}Ni_{5.3}P_{22.5}$ alloy that were identically prepared except for their *in situ* hold times of 3, 20, 30, and 40 min, respectively. First, a comparison of topographical AFM images (Fig. 1a–d) reveals that all four samples exhibit similar terraced structures. Thereby, samples with a holding time of 3 min (Fig. 1a) are known to yield fully amorphous replica of their STO molds whose surfaces reflect an exact mirror image of the original terraced structure of the STO, including a precise reproduction of the STO step height of 0.39 nm [19]. However, the imprinted samples with longer holding time, Fig. 1b–d, also have clear terraced structures similar to the one of Fig. 1a despite being held at elevated temperature for much longer than the typical thermoplastic forming window of Pt-BMG of ≈15 min [19], which suggests that their ability to mold the original STO substrate's surface structure is comparable with the one exhibited by the 3-min imprint, Fig. 1a. This conclusion is corroborated by an analysis of the on-terrace surface roughness, which was found to be less than 1 Å for all three samples. To quantify the quality of the replication, line profiles corresponding to the colored lines marked in Fig. 1a–d are extracted from the topographical data
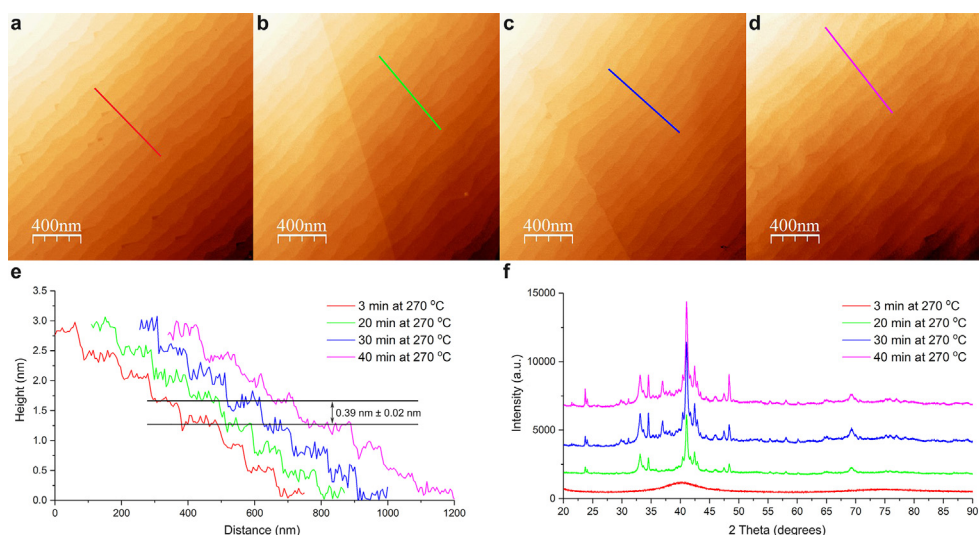
Fig. 1. (a)–(d) Topographical atomic force microscope images of samples prepared from Pt-BMG as described and then held at 270 °C for (a) 3 min; (b) 20 min; (c) 30 min; and (d) 40 min. All images reveal well-defined terraced surface structures with surface roughness less than 1 Å RMS. (e) Line profiles taken along the colored lines indicated in (a)–(d). Steps between terraces are found to be 0.39 nm ± 0.02 nm in height for all samples, which precisely matches the dimension of one unit cell of the STO crystal used as a mold. (f) X-ray diffraction spectra of the four samples. owing to the absence of any peaks, the sample heated for 3 min (red curve) is confirmed to be fully amorphous while the other three samples feature clear peaks stemming from at least partial crystalline order.

(Fig. 1e). Evidently, all four profiles reflect the terraced structure of the samples with step heights of 0.39 nm ± 0.02 nm separating them, with little or no loss of accuracy for samples kept longer at maximum temperature even though steps for the 40-min sample appear to be somewhat less sharp than for the other three samples.

To check the expectation that the sample kept at 270 °C for 3 min is amorphous while the other three are crystalline, XRD has been carried out. From the spectra plotted in Fig. 1f, we see that all three samples exposed to the long hold times generate clear crystallization peaks while there is only an amorphous bump at a 2 theta angle of around 40° for the sample with 3 min of hold time. We can nevertheless distinguish the three samples featuring crystalline peaks in that the one held for 20 min was only partially crystallized. This conclusion is evidenced by the fact that the XRD curves of samples held for at least 30 min have more and better developed peaks, suggesting there is further crystallization or phase transformation yet to come for the 20-min sample. In contrast, the XRD spectra of the 30 min and the 40 min holding time samples are almost identical, indicating that the imprinted $Pt_{57.5}Cu_{14.7}Ni_{5.3}P_{22.5}$ alloy may become virtually fully crystallized after being held at 270 °C for 30 min or longer. This conjecture is further supported by isothermal measurements using differential scanning calorimetry (DSC), which confirm that phase transformations are completed after about 23 min of total hold time (Supplemental Fig. 1). All combined, we find that the $Pt_{57.5}Cu_{14.7}Ni_{5.3}P_{22.5}$ alloy retains its superior replication capabilities even if kept at 270 °C for twice the time it takes for the material to crystallize.

Complementing the findings from the XRD and DSC results discussed earlier, which represent bulk property measurements, surface characterization by AFM also hints at the occurrence of a phase transition in the longer annealed samples. This is illustrated in Fig. 2, where it is shown that when imprinted with the identical STO crystal, similarly looking terraced structures result as topography for both a 40-min sample (Fig. 2a) and a 3-min sample (Fig. 2b) even though the 3-min sample is amorphous while the other one is crystalline. From the phase images Fig. 2c and d, however, it became clear that for the 40-min sample, two distinct phases are present, as revealed by the lighter orange and the darker
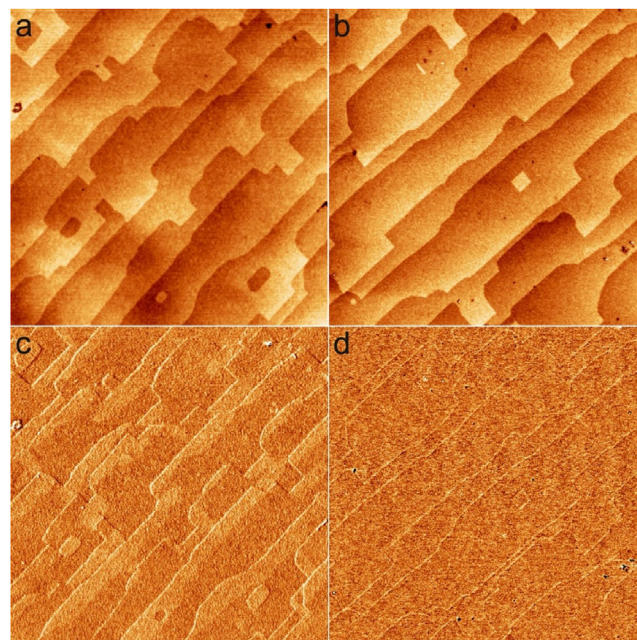

Fig. 2. (a)–(b) Topographical AFM images of replica made from Pt-BMG at 270 °C with (a) 40 min and (b) 3 min hold time, respectively, using the same STO crystal as mold. (c)–(d) Phase images corresponding to the topographical images in (a) and (b). Image sizes are 2 μm × 2 μm in all cases.

orange appearance, while there is only one (amorphous) phase visible for the 3-min sample. Because the existence of a phase contrast in tapping mode AFM indicates locally different energy dissipation properties of the oscillating cantilever, which on otherwise flat samples may be caused by locally different visco-elastic properties, changes in adhesion, and variations in the maximum tip-sample contact area during an individual tap [32,33], any changes in a sample's structural phase that would result in a visible phase contrast would need to occur at the surface itself. Most notable, whatever the phase change comprises, its

manifestation is influenced by the existence of surface steps, along which the phases align.

To further investigate the occurrence of phase separation, viscoelastic mapping was conducted by the contact resonance method to visualize storage modulus differences [30,34−37]. Fig. 3a−c shows the topography of samples imprinted at 270 °C for 3 min, 20 min, and 40 min, respectively; as expected from the earlier presented results, they show no significant difference in the surface's overall appearance. Similarly, the viscoelastic image of the sample that has been annealed for 3 min is featureless except for some artifacts along the step edges that generate some white dots, confirming that the sample's amorphous bulk phase is structurally homogeneous (Fig. 3d). This is in full agreement with the phase image Fig. 2d, which was also featureless. However, for the two samples that were annealed for 20 min and 40 min, respectively, areas representing at least two distinct moduli are measured, with brighter colors indicating higher storage modulus. Most notably, domains representing the same storage modulus extend across terraces, unlike the phase differences revealed by Fig. 2c.

Although the aforemntioned results clearly point to the existence of multiple phases near the surface for the samples that have been annealed until crystallization, they cannot clarify whether these are crystal-crystal (with different crystalline structures) or crystal-amorphous. To further investigate this issue, cross-sectional TEM imaging was performed using a 40-min sample that was prepared into a thin lamella by focused ion beam milling. As shown in Fig. 4a, a distinguishable surface layer with uniform contrast is observed, which has been separated with a white dashed line to guide the eye. To investigate this layer in detail, atomic-resolution TEM imaging has been carried out at the location marked with the black box. In the respective micrograph Fig. 4b, lattice fringes are visible in the material that is more than ≈15 nm away from the surface (region A) while at closer distances, the sample looks like mostly crystalline clusters of a couple of nanometers in diameter (regions B a C) that have been distributed within a matrix D that is predominantly disordered.

To further clarify the structural nature of this surface layer, we conducted high-angle annular dark-field scanning transmission electron microscopy (HAADF-STEM) imaging in combination with nanobeam electron diffraction (NBED) measurements using a ≈2.5 nm-wide electron beam with convergent angle of 0.6 mrad. First, the HAADF-STEM image in Fig. 4c again confirms the existence of a distinct surface layer of about 15−20 nm thickness, from which a uniform contrast is observed, while noticeable lattice fringes are shown in the bulk region. The NBED patterns shown at the right side of Fig. 4d have then been acquired by moving the electron beam across the region covered by the semitransparent rectangle in the HAADF-STEM image on the left side of the image. From the obtained diffraction patterns, patterns acquired from 'deep' inside the sample (i.e., >20 nm away from the replicated surface) show multiple diffraction peaks indicating a polycrystalline structure, while patterns taken within 20 nm of the surface reveal a mix of both crystalline and amorphous features. Finally, diffraction patterns acquired within the protective carbon layer feature amorphous rings, as expected, but note that the amorphous rings observed in the diffraction patterns near the surface of the sample are distinct from the amorphous rings from the carbon layer. Thus, the combination of the results from Fig. 4 confirm that any material located more than ≈15−20 nm away from the replicated surface is likely fully crystalline, although still multiple different crystalline phases may occur.

For material that is closer than ≈15−20 nm to the surface, the situation is more complicated. This finding can be looked at as unusual as one could assume that the presence of the STO mold would generate a heterogeneous nucleation environment for the Pt-BMG alloy where the material would nucleate faster at the surface than inside the bulk, which would ultimately lead to crystallization starting from the surface growing towards the bulk. On the other hand, this effect may be precisely what gives rise to the formation of the numerous mostly crystalline clusters located within the surface layer. Nevertheless, the structural differences between the mostly crystalline clusters B/C and the matrix D at
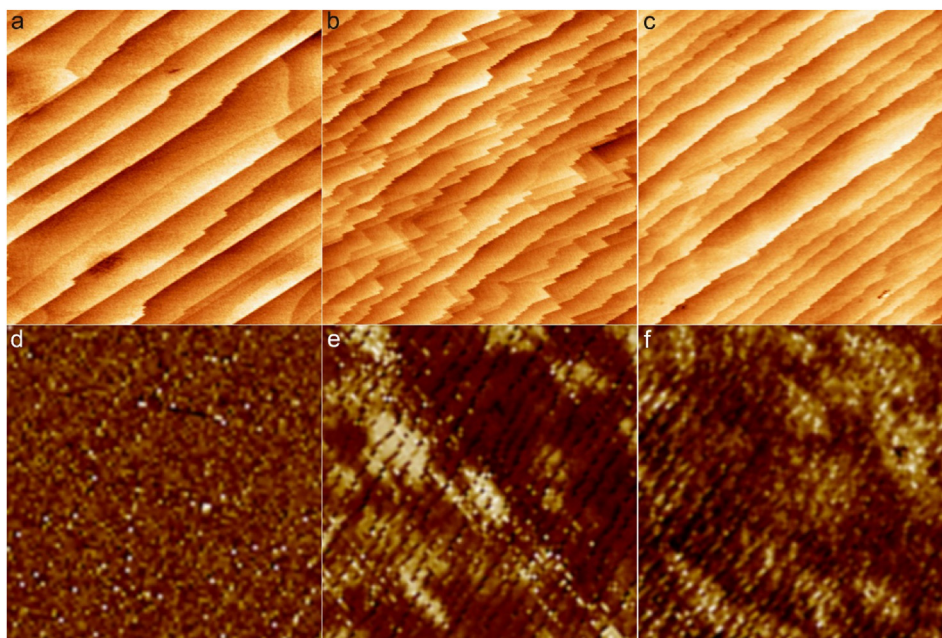

Fig. 3. (a)−(c) AFM topography images of Pt-BMG samples imprinted at 270 °C and then held under pressure at that temperature for (a) 3 min, (b) 20 min, and (c) 40 min. (d)−(f). Storage modulus (E') images from viscoelastic mapping carried out on the same three samples but on different locations, with (d) representing the 3-min sample, (e) the 20-min sample, and (f) the 40-min sample. Thereby, no contrast is observed on the 3-min sample, indicating structural homogeneity of the bulk. In contrast, brighter and darker areas in (e) and (f) reveal the existence of domains that vary in storage modulus and spread across multiple terraces. All images are 2 μm × 2 μm in size.
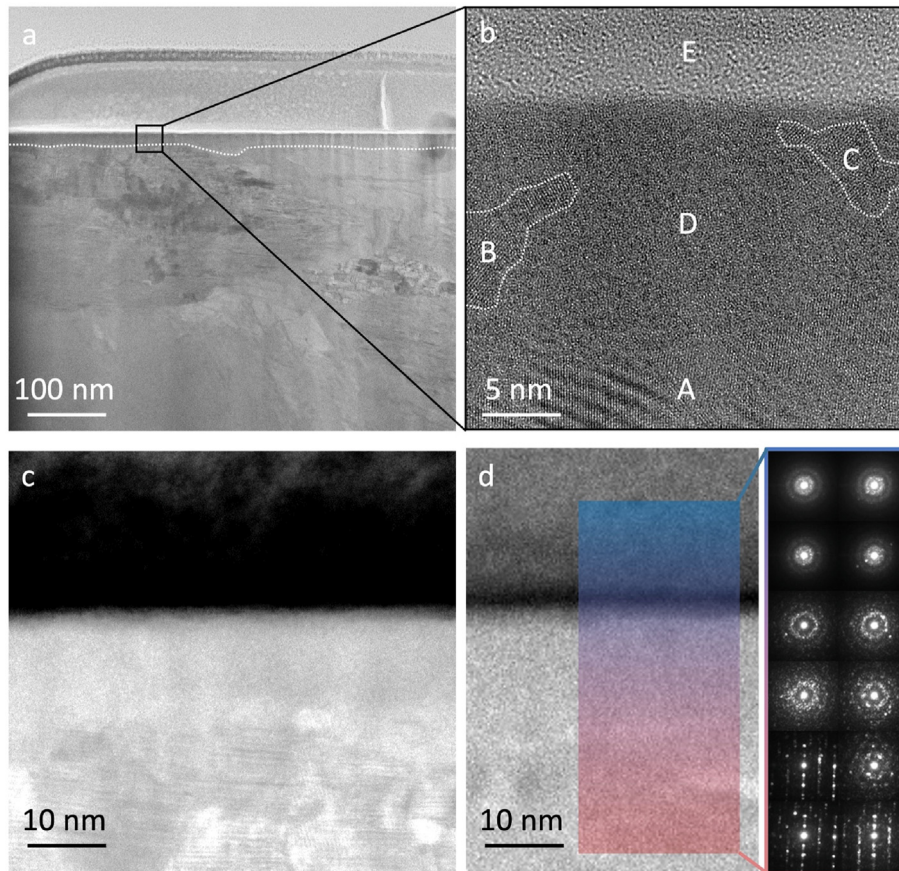
Fig. 4. (a) Cross-sectional TEM image of a 40-min sample where a partially amorphous surface layer has been highlighted with white dash line. (b) A zoom-in atomic-resolution TEM image from the area marked with the black box in (a). Different areas of crystalline or mostly crystalline order inside the Pt-BMG alloy are labeled with A, B, and C, while the surface layer D is mostly disordered. The area E represents the amorphous carbon layer covering the sample to preserve the surface structure of the sample. (c) HAADF-STEM image of the 40-min sample showing the mostly amorphous surface layer with a thickness of around 15−20 nm. (d) HAADF-STEM image with corresponding NBED patterns obtained at the respective locations located within the color gradient box.

places where the clusters B/C are located right at the surface may very well explain the contrast found in the phase image of Fig. 2c while the storage modulus domains of Fig. 3e−f may be influenced by the occurrence of different crystalline phases located in the region deeper than 15 nm.

Based on the results presented thus far, we are now able to develop a more detailed picture of what happens during the extended hold times at 270 °C. Usually, heterogeneous nucleation would dominate the beginning of the crystallization process from a liquid state; thus, areas with the ability to heterogeneously nucleate (here: the alloy-mold interface) should crystallize earlier than the other areas. However, this process may not be valid for bulk metallic glasses in their supercooled liquid state because such a state is characterized by viscosities that are orders of magnitude larger than for standard liquids. This results in a much lower mobility of atoms that makes local compositional rearrangement harder, which is nevertheless required for multicomponent BMG to crystallize as these alloys usually consist of specific combinations of atomic species that have especially high resistance of crystallization. This general intricacy is paired with the fact that lattice mismatch prevents the crystallized alloy to perfectly conform with the surface structure of the mold, which creates an energy barrier required to 'unmatch' the atoms at the alloy-mold interface during crystallization, in particular when pressure is exerted to the system by the press that pushes the alloy atoms towards the mold surface [38]. In addition, when the bulk areas

beneath the surface layer become increasingly crystallized, mass transfer from the bulk to the surface slows and may ultimately become negligible. As a result, the 15−20-nm-thick surface layer is caught between a fully crystallized interior and the confinement provided by the mold with the thermal energy at 270 °C being insufficient to overcome the related energetic barriers toward creating long-range order, thereby effectively locking in an amorphous zone.

The surface layer's resistance to crystallization goes, however, beyond overcoming an energetic barrier imposed by pressure and confinement. Instead, even when both are relieved, the top layer displays an astonishing stability. This is explored in the experiments described in Fig. 5, where the surface evolution during _ex situ_ annealing is investigated. The specific sample shown was first imprinted at 270 °C, but after 3 min of hold time, the temperature was increased to 450 °C for five more minutes. This was carried out because compared with samples heated to 270 °C only, samples annealed at 450 °C or higher have experienced all possible phase transformations and are expected to have reached their lowest energy state (see Supplemental Fig. 2), thereby ensuring that material located beneath the surface layer will not undergo any further phase transformations even though structural features such as grain sizes and shapes of boundaries may still change. This allows the best possible insight into the behavior of the surface layer during the _ex situ_ heating process as bulk changes ought to be minimized.
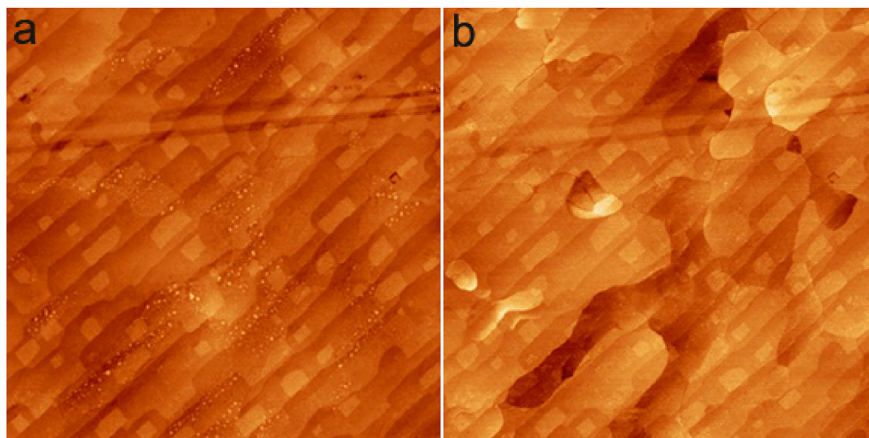
Fig. 5. (a) Topographical AFM image of a Pt-BMG sample imprinted at 270 °C and then, after an initial hold time of 3 min, kept at 450 °C for an additional 5 min. Before the measurement, it had been stored in ambient conditions for 1 week. (b) AFM image of the same location after the sample had been annealed at 450 °C for 5 min in a differential scanning calorimeter protected by argon gas. Both images are 4 μm × 4 μm in size.

We start with the image Fig. 5a, which shows an area on the sample prepared as described earlier, but which was afterward being stored in ambient condition for one week before the measurement was conducted. Despite contaminations that are either particles deposited from the air or local surface oxidation, which manifest as bright dots in parts of the image, the sample shows the same terraced structure as usual (in this case including a good number of on-terrace islands, which originate from an above average number of etch pits that were present in the particular STO crystal used as mold). After 5 min of *ex situ* annealing at 450 °C, AFM imaging was repeated at the same spot (Fig. 5b). The terraced surface structure remained largely unchanged even though areas that displayed surface contamination appear to be prone to the formation of depressions or trenches, indicating that the contaminations act as nucleation centers. This stability and resistance against full crystallization can be viewed as somewhat surprising because *ex situ* annealing of samples that were identically prepared except for the 5 min hold time at 450 °C leads to a complete disappearance of imprinted features and a significant surface roughening [27]. For comparison, we also conducted a similar experiment with a sample that was first annealed *in situ* for 30 min at 270 °C followed by *ex situ* heating at the same temperature for an additional 30 min (Supplemental Fig. 3). Although significant recrystallization occurred inside the bulk that manifest as elevated leaf-shaped domains, the surface layer was again found to be astonishingly resilient.

4. Conclusions

This work establishes a novel way of imprinting features onto crystalline materials at the atomic scale, as demonstrated by the replication of the terraced surface structure of ⟨100⟩-oriented strontium titanate single crystals with subangstrom accuracy. Thereby, the presence of a largely disordered surface layer of $\approx 15-20$ nm thickness, which remains in place even after the bulk has fully crystallized, does not only allow the $Pt_{57.5}Cu_{14.7}Ni_{5.3}P_{22.5}$ alloy used for forming to break the intrinsic limitations usually imposed by grain size and/or crystal structure but also is expected to improve many of the sample's mechanical and chemical properties if compared with fully crystalline samples. On the other hand, replicas show an astonishing resiliency to postpreparation annealing that is superior to the one exhibited by fully amorphous imprints made from the same alloy. Because this method of imprinting at the angstrom scale is easy to implement while

yielding surfaces that are more stable than their glassy counterparts, it could be applied to device-scale demonstrations that require robust metallic materials patterned with high accuracy at the nanometer scale.

Credit author statement

Declaration of competing interest

The authors declare that they have no known competing financial interests or personal relationships that could have appeared to influence the work reported in this paper.

Acknowledgments

Appendix A. Supplementary data

Supplementary data to this article can be found online at https://doi.org/10.1016/j.mtnano.2021.100145.

References

[1] L.J. Guo, Nanoimprint lithography: methods and material requirements, Adv. Mater. 19 (4) (2007) 495−513.
[2] D.R. Barbero, M.S.M. Saifullah, P. Hoffmann, H.J. Mathieu, D. Anderson, G.A.C. Jones, M.E. Welland, U. Steiner, High resolution nanoimprinting with a robust and reusable polymer mold, Adv. Funct. Mater. 17 (14) (2007) 2419−2425.
[3] J.P. Singer, M. Gopinadhan, Z. Shao, A.D. Taylor, J. Schroers, C.O. Osuji, Nanoimprinting sub-100 nnn features in a photovoltaic nanocomposite using durable bulk metallic glass molds, ACS Appl. Mater. Interfaces 7 (6) (2015) 3456−3461.
[4] S.Y. Chou, C. Keimel, J. Gu, Ultrafast and direct imprint of nanostructures in silicon, Nature 417 (6891) (2002) 835−837.

[5] Y.W. Hu, P. Kumar, R. Xu, K.J. Zhao, G.J. Cheng, Ultrafast direct fabrication of flexible substrate-supported designer plasmonic nanoarrays, Nanoscale 8 (1) (2016) 172—182.

[6] S.Y. Chou, P.R. Krauss, P.J. Renstrom, Imprint lithography with 25-nanometer resolution, Science 272 (5258) (1996) 85—87.

[7] C. Zhou, A. Datye, Z. Chen, G.H. Simon, X.Z. Wang, J. Schroers, U.D. Schwarz, Atomic imprinting in the absence of an intrinsic length scale, Apl. Mater. 8 (11) (2020).

[8] L.M. Cox, A.M. Martinez, A.K. Blevins, N. Sowan, Y.F. Ding, C.N. Bowman, Nanoimprint lithography: emergent materials and methods of actuation, Nano Today 31 (2020).

[9] R.W. Jaszewski, H. Schift, J. Gobrecht, P. Smith, Hot embossing in polymers as a direct way to pattern resist, Microelectron. Eng. 42 (1998) 575—578.

[10] B.D. Gates, G.M. Whitesides, Replication of vertical features smaller than 2 nm by soft lithography, J. Am. Chem. Soc. 125 (49) (2003) 14986—14987.

[11] G. Kumar, H.X. Tang, J. Schroers, Nanomoulding with amorphous metals, Nature 457 (7231) (2009) 868—872.

[12] H. Gao, Y.W. Hu, Y. Xuan, J. Li, Y.L. Yang, R.V. Martinez, C.Y. Li, J. Luo, M.H. Qi, G.J. Cheng, Large-scale nanoshaping of ultrasmooth 3D crystalline metallic structures, Science 346 (6215) (2014) 1352—1356.

[13] Z. Liu, One-step fabrication of crystalline metal nanostructures by direct nanoimprinting below melting temperatures, Nat. Commun. 8 (2017).

[14] A. Sharstniou, S. Niauzorau, P.M. Ferreira, B.P. Azeredo, Electrochemical nanoimprinting of silicon, P. Natl. Acad. Sci. USA 116 (21) (2019) 10264—10269.

[15] F. Hua, Y.G. Sun, A. Gaur, M.A. Meitl, L. Bilhaut, L. Rotkina, J.F. Wang, P. Geil, M. Shim, J.A. Rogers, A. Shim, Polymer imprint lithography with molecular-scale resolution, Nano Lett. 4 (12) (2004) 2467—2471.

[16] P. Nagpal, N.C. Lindquist, S.H. Oh, D.J. Norris, Ultrasmooth patterned metals for plasmonics and metamaterials, Science 325 (5940) (2009) 594—597.

[17] S. Elhadj, R.M. Rioux, M.D. Dickey, J.J. DeYoreo, G.M. Whitesides, Sub-nanometer replica molding of molecular steps on ionic crystals, Nano Lett. 10 (10) (2010) 4140—4145.

[18] J.M. Yao, A.P. Le, M.V. Schulmerich, J. Maria, T.W. Lee, S.K. Gray, R. Bhargava, J.A. Rogers, R.G. Nuzzo, Soft embossing of nanoscale optical and plasmonic structures in glass, ACS Nano 5 (7) (2011) 5763—5774.

[19] R. Li, Z. Chen, A. Datye, G.H. Simon, J. Ketkaew, E. Kinser, Z. Liu, C. Zhou, O.E. Dagdeviren, S. Sohn, J.P. Singer, C.O. Osuji, J. Schroers, U.D. Schwarz, Atomic imprinting into metallic glasses, Commun. Phys. 1 (1) (2018) 75.

[20] Z. Chen, A. Datye, G.H. Simon, C. Zhou, S.A. Kube, N.J. Liu, J.B. Liu, J. Schroers, U.D. Schwarz, Atomic-scale imprinting by sputter deposition of amorphous metallic films, ACS Appl. Mater. Interfaces 12 (47) (2020) 52908—52914.

[21] Y. Akita, T. Watanabe, W. Hara, A. Matsuda, M. Yoshimoto, Atomically stepped glass surface formed by nanoimprint, 12-16, Jpn. J. Appl. Phys. 2 (46) (2007) L342—L344.

[22] Y. Miyake, Y. Akita, H. Oi, M. Mita, S. Kaneko, K. Koyama, K. Sunagawa, K. Tada, Y. Hirai, M. Yoshimoto, Nanoimprint fabrication and thermal behavior of atomically ultrasmooth glass substrates with 0.2-nm-Height steps, Jpn. J. Appl. Phys. 50 (7) (2011).

[23] O. Suga, M. Yoshimoto, C. Okuyama, A. Matsuda, H. Hiroshima, M. Takahashi, Atomic step patterning on quartz glass via thermal nanoimprinting, Jpn. J. Appl. Phys. 54 (9) (2015).

[24] A. Inoue, Stabilization of metallic supercooled liquid and bulk amorphous alloys, Acta Mater. 48 (1) (2000) 279—306.

[25] C.A. Schuh, T.C. Hufnagel, U. Ramamurty, Overview No.144 - mechanical behavior of amorphous alloys, Acta Mater. 55 (12) (2007) 4067—4109.

[26] O.E. Dagdeviren, G.H. Simon, K. Zou, F.J. Walker, C. Ahn, E.I. Altman, U.D. Schwarz, Surface phase, morphology, and charge distribution transitions on vacuum and ambient annealed SrTiO3(100), Phys. Rev. B 93 (19) (2016).

[27] Z. Chen, A. Datye, J. Ketkaew, S. Sohn, C. Zhou, O.E. Dagdeviren, J. Schroers, U.D. Schwarz, Relaxation and crystallization studied by observing the surface morphology evolution of atomically flat Pt57.5Cu14.7Ni53P22.5 upon annealing, Scripta Mater. 182 (2020) 32—37.

[28] J.X. Yu, A. Datye, Z. Chen, C. Zhou, O.E. Dagdeviren, J. Schroers, U.D. Schwarz, Atomic-scale homogeneous plastic flow beyond near-theoretical yield stress in a metallic glass, Commun. Mater. 2 (1) (2021).

[29] S. Woo, H. Jeong, S.A. Lee, H. Seo, M. Lacotte, A. David, H.Y. Kim, W. Prellier, Y. Kim, W.S. Choi, Surface properties of atomically flat poly-crystalline SrTiO3, Sci Rep-Uk 5 (2015).

[30] U. Rabe, W. Arnold, Acoustic microscopy by atomic-force microscopy, Appl. Phys. Lett. 64 (12) (1994) 1493—1495.

[31] B. Pittenger, D.G. Yablon, Quantitative Measurements of Elastic and Visco-elastic Properties with FASTForce Volume CR, Bruker Corporation, 2017.

[32] P. Eaton, P. West, Oxford University Press, Atomic Force Microscopy, Oxford University Press, Oxford, 2010, p. 1, online resource (viii, 248 pp.).

[33] R. Castro García, Amplitude Modulation Atomic Force Microscopy, Wiley VCH, Weinheim, Chichester, 2010.

[34] U. Rabe, V. Scherer, S. Hirsekorn, W. Arnold, Nanomechanical surface characterization by atomic force acoustic microscopy, J. Vac. Sci. Technol. B 15 (4) (1997) 1506—1511.

[35] B. Bendjus, B. Kohler, H. Heuer, U. Rabe, A. Striegler, Determination of deformation fields by atomic force acoustic microscopy, Proc. SPIE 6175 (2006) U134—U143.

[36] K. Yamanaka, H. Ogiso, O. Kolosov, Ultrasonic force microscopy for nanometer resolution subsurface imaging, Appl. Phys. Lett. 64 (2) (1994) 178—180.

[37] P.A. Yuya, D.C. Hurley, J.A. Turner, Contact-resonance atomic force microscopy for viscoelasticity, J. Appl. Phys. 104 (7) (2008).

[38] H.T. Zhang, Y.F. Mo, Z.A. Tian, R.S. Liu, L.L. Zhou, Z.Y. Hou, The effect of pressure on the crystallization of rapidly supercooled zirconium melts, Phys. Chem. Chem. Phys. 19 (19) (2017) 12310—12320.